Catalysis Today xxx (xxxx) xxx–xxx

Contents lists available at ScienceDirect

Catalysis Today

journal homepage: www.elsevier.com/locate/cattod

Novel porous ceramic sheet supported metal reactors for continuous-flow catalysis

Qijie Jin[a,b,c], Bingxu Lu[a,b], Youchun Pan[a,b], Xingjun Tao[a,b], Cindy Himmelhaver[c], Yuesong Shen[a,b,*], Sasa Gu[a,b], Yanwei Zeng[a], XiuJun Li[c,*]

[a] College of Materials Science and Engineering, Nanjing Tech University, Nanjing 210009, China
[b] Jiangsu Collaborative Innovation Center for Advanced Inorganic Function Composites, Nanjing Tech University, Nanjing, 210009, China
[c] Department of Chemistry and Biochemistry, Environmental Science & Engineering, and Biomedical Engineering, University of Texas at El Paso, El Paso, TX, 79968, USA

ARTICLE INFO

Keywords:
Porous ceramic
Nickel
Continuous-flow
Catalysis
Environmental degradation

ABSTRACT

A novel porous ceramic sheet supported nickel particles reactor was obtained by an *in-situ* preparation method. This reactor was then used to investigate continuous-flow catalysis of nitroaromatic compounds and methyl orange. The details of the structure and morphology were characterized by XRD, SEM, XPS, Raman, element mapping, mercury intrusion method and Archimedes principle. The porous ceramic sheet supported Ni particles reactor exhibited excellent catalytic performance in the catalytic reduction of *p*-nitrophenol and methyl orange by sodium borohydride at room temperature. Both the conversion of *p*-nitrophenol (5 mM) and methyl orange (0.3 mM) reached nearly 100% at the injection speed of 2.67 mL·min^{-1}. In addition, it maintained conversions of 100% after 10 recycling time since the porous ceramic sheet could reduce the aggregation for Ni particles. Furthermore, the chemisorbed oxygen, and the strong interaction between Ni and porous ceramic sheet resulted in a highly efficient, recoverable, and cost-effective multifunctional reactor. All of these advantages present new opportunities to be implemented in the field of waste water treatment and environmental toxicology. Ultimately, the porous ceramic sheet could also support other metal nanomaterial, and used in other fields of environmental catalysis.

1. Introduction

The catalysis, especially heterogeneous catalysis combined with the traditional batch reactor, is an essential technology for modern chemical industry [1–3]. However, many disadvantages exist in the traditional batch reactor, such as low efficiency, concentration gradients, poor heat transfer and etc. [4]. In contrast, the continuous-flow (CF) presents great potential to researchers due to its high operability, ease of reaction control, automation, and ability for scale up [5]. It exhibits higher efficiency, better quality, and greater sustainability in many fields, such as green synthesis [6], heart failure treatment [7,8], microfluidics [9], catalysis [10,11] and etc. These advantages guarantee that the CF forms an excellent alternative technology to replace the traditional batch reactor [12–14]. Simply, the combination of CF with heterogeneous catalysis has many unparalleled advantages and is increasingly becoming the powerful tool in the modern chemical industry. The development of CF in heterogeneous catalysis possesses is of significant value economically and in the field of research.

Nanomaterials have been extensively investigated due to the unique size, large surface-area-to-volume ratios, and shape effect [15–21]. Metal nanocatalyst, an important member of nanomaterials, has increasing applications in various fields [22]. For instance, the aqueous Au-Pd colloids are used to catalyze selective CH_4 oxidation to CH_3OH [23]; the $Au_{25}(SG)_{18}$ nanoclusters are used for photothermal therapy [24]; and the nickel nanoparticles (NiNPs) loaded cellulose filter paper is used for the *p*-nitrophenol (4-NP) reduction [25]. Among these applications, environmental catalysis, especially in the field of water treatment, has gained attention due to the increase of stringent environmental regulations. Currently, Au/TiO_2 [26], AgNPs/SiNSs [27], Pt-Fe_3O_4@graphene [28] and many other metal nanocatalysts have been used for water treatment. Presently, the technology combination of noble metal nanocatalysis with CF exhibits obvious advantages (high reaction efficiency and reproducibility) in the field of water treatment [29]. However, one current challenge in designing the metal catalyst (anchored within CF reactors) is to improve catalytic efficiency and reusability synchronously. For example, for the 4-NP reduction, the Pd/UiO-66-NH_2 film capillary microreactor can be reused readily but its maximum flow rate is just 60 μL·min^{-1} [30]. In another example, the

* Corresponding authors.
E-mail addresses: sys-njut@163.com (Y. Shen), xli4@utep.edu (X. Li).

https://doi.org/10.1016/j.cattod.2019.12.006
Received 4 March 2019; Received in revised form 16 November 2019; Accepted 2 December 2019

Au nanoparticles (AuNPs) anchored paper reactor can exhibit high catalytic efficiency at a flow rate of 0.25 mL·min^{-1} but the cellulose of paper would be gradually destroyed in an alkaline environment [15]. With this in mind, intensive research of the catalyst is imperative for low cost and high catalytic efficiency for metal nanocatalysis.

As an active ingredient, nickel is the excellent electron-donor or acceptor resulting in the capacity to promote the catalytic reaction by the redox cycle process significantly. Therefore, Ni material has great advantages in the catalytic reaction [31,32]. High cost is one of the hurdles for commercialization of noble metals. Nickel has appeared as a considerable alternative. Therefore, the presence of Ni particles provides a possibility for increasing the catalytic efficiency and reusability simultaneously in the field of water treatment. Recently, various materials have been used for the carriers, such as graphene oxide [33], TiO_2 [34,35], polymer [36] and cellulose [37]. As an emerging catalyst carrier, porous ceramic sheet (PCS) has a continuous pore structure (micro-sized diameter) featuring high porosity, offering easily accessible active sites. The strong interaction between Ni particles and PCS (contains Al_2O_3 and SiO_2) can also exist. Both of these factors are beneficial for the improvement of catalytic efficiency. Furthermore, the PCS has excellent chemical inertness so it can exist stably in a strong alkaline condition. The strong interaction guarantees that the NiNPs are not easily separated from the PCS, which enhances the reusability for the catalyst, indicating that the PCS supported Ni particles (Ni/PCS) possess high catalytic efficiency and high reusability in the field of water treatment.

In order to prove the high catalytic efficiency and reusability of PCS supported Ni particles, the catalytic reduction of 4-NP and methyl orange (MO) were chosen as a model in the water treatment field. It is well known that 4-NP and MO are important contributors to worsening environment problems such as water contamination and result in mutagens, teratogens, carcinogens, etc. [38]. Alternatively, *p*-aminophenol (4-AP) is an important intermediate with widespread applications in various fields, including the antipyretic drugs, photographic developer, corrosion inhibitor and hair-dying agent [39–41]. With the improvement of environmental protection awareness and the increasingly strict environmental protection laws [28], developing technology to degrade organic pollutant has great ecological environmental significance and important economic value [42,43].

Herein, we report an efficient approach to synthesize the Ni/PCS catalyst and fabricate it as a continuous-flow reactor. The Ni/PCS reactor exhibited higher catalytic efficiency and higher reusability than various continuous-flow catalysts. Both the conversion of 4-NP and MO reached nearly 100% at the injection speed of 2.67 mL·min^{-1} while the catalytic efficiency exhibited no great change after 10 recycling times.

2. Experiment

2.1. Catalyst preparation and reactor fabrication

All the details about materials and chemicals for catalyst preparation were provided in Supporting Information (SI). Scheme 1 represented the Ni/PCS preparation and the reactor fabrication. The Ni/PCS catalyst was synthesized by an *in-situ* preparation method, which was versatile in the preparation of PCS supported metal catalyst. First, alumina fiber (56.0 wt.%), glass powder (24.0 wt.%), activated carbon powder (10.0 wt.%), wood powder (10.0 wt.%) and appropriate amount of deionized water were mixed and pelletized. Then, the hybrid material was combined in a cylinder (diameter of 22 mm, thickness of 10 mm) and calcined at 1100 ℃ for 2 h. Next, $NiCl_3{\cdot}6H_2O$ was added into deionized water to obtain the $NiCl_3$ green clarified solution. The PCS was immersed to 2 mL $NiCl_3$ solution for 1 h allowing self-assembly of the Ni^{2+} in the PCS. Then, the PCS (absorbed Ni^{2+}) was added into 50 mL sodium borohydride (1 M) so that the Ni particles were self-assembly in the PCS. Its chemical reaction was $Ni^{2+} + BH_4^- + 2H_2O \rightarrow Ni^0 + BO_2^- + 2H^+ + 3H_2$. In the next step, the sample was washed with deionized water and dried to obtain the Ni/PCS catalyst. Finally, the Ni/PCS catalyst was assembled into a quartz tube (22 mm inner diameter, 60 mL) and the Ni/PCS reactor was obtained. The resulting concentrations of $NiCl_3$ were 0.10 M, 0.25 M, 0.50 M, 0.75 M and 1.00 M, respectively, which were denoted as Ni/PCS-1, Ni/PCS-2, Ni/PCS-3, Ni/PCS-4 and Ni/PCS-5, respectively.

2.2. Catalytic activity measurement

The catalytic efficiency of the Ni/PCS reactor was investigated by the two reactions: (1) MO conversion to N,N-dimethylbenzene-1,4-diamine (DPD) and 4-aminobenzenesulfonic acid (ABA); (2) 4-NP conversion to 4-AP. As an example of 4-NP conversion to 4-AP, a typical procedure was adopted for carrying out the chemical reaction. The 4-NP solution (0.5 − 6 mM, 20 mL) and $NaBH_4$ solution (0.1 M, 20 mL) were added to the beaker and mixed together. Then, the mixed solution (40 mL) was added into the Ni/PCS reactor and the height of the mixed solution was kept by a micro-injection pump. With the reaction progress, the reacted liquid was collected by the beaker. The value of TOC was collected by the total organic carbon analyzer. Afterwards, 2 mL mixed solutions were pumped in cuvette. The cuvette was placed in a UV–vis spectrophotometer to measure the absorbance spectra. The conversion of 4-NP (X) was calculated by the Eq. (1).

$$X = (C_0\text{-}C_t)/C_0 \times 100\% \quad (1)$$

The C_0 was the initial 4-NP concentration and C_t was the concentration at different time interval (t). Furthermore, the Ni/PCS catalyst was recycled to investigate the reusability. For every recycling, the used catalyst was washed and vacuum dried for the next experiment. The similar procedure was employed for the MO reduction. The initial concentrations of MO and $NaBH_4$ were 0.3 mM and 30 mM, respectively.

2.3. Characterization

X-ray diffraction (XRD) patterns were obtained on an X-ray diffractometer (Smartlab TM 9Kw, Rigaku, Japan). The 2θ scans covered the range 10 ~ 80 °, and the accelerating voltage and applying current were 45 kV and 200 mA, respectively. The microstructural natures and element mapping of the catalysts were investigated using a scanning electron microscope (JEOL, JSM-5900). Visible Raman spectra of the catalysts were collected at room temperature on the LabRAMHR800 (Horiba Jobin Yvon). A 514 nm diode-pumped solid-state semiconductor laser was used as the excitation source with a power output of 30 mW. The spectra were recorded over the range of 100-1200 cm^{-1} with a resolution of 0.5 cm^{-1}. The X-ray photoelectron spectroscopy (XPS) patterns were acquired by the PHI 5600 spectrometer with a hemispherical energy analyzer (Mg-Kα radiation, 1253.6 eV at 100 W), and the vacuum degree was maintained at 10^{-7} Pa. The samples were dried at 80 °C for 24 h to remove moisture and then were tested without surface treatment. Curve fitting was performed by utilizing XPSPEAK 4.1 with a Shirley-type background. Archimedes principle was employed to measure the bulk density (D), apparent porosity (P) and water absorption (W). The sample was dried at 120 ℃ for 5 h and the weight was denoted as M_1. The sample was immersed to deionized water and brought to a boil. The gravity of the sample was denoted as M_2 when the water cooled down to room temperature. The water on the sample surface removed using a water absorbing sponge and the weight of the sample was denoted as M_3. The D, P and W were calculated by the Eq. (2) – (4).

$$D = M_1/(M_3\text{-}M_2) \times 100\% \quad (2)$$

$$W = (M_3\text{-}M_1)/M_1 \times 100\% \quad (3)$$

$$P = (M_3\text{-}M_1)/(M_3\text{-}M_2) \times 100\% \quad (4)$$

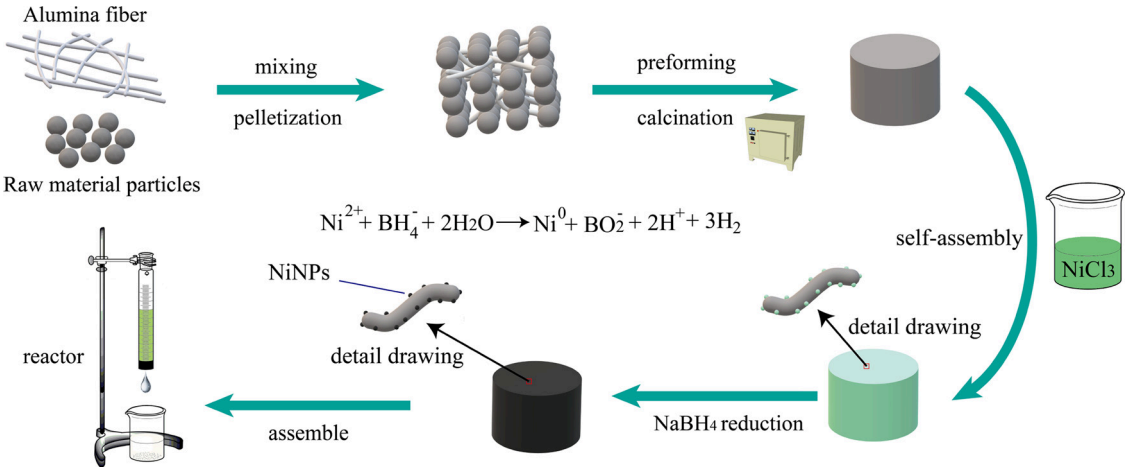

Scheme 1. Preparation and fabrication of the Ni/PCS reactor.

3. Results and discussion

3.1. Physical structure and properties

Fig. 1 showed XRD patterns and SEM micrographs of PCS sponge and Ni/PCS reactors. Fig. 1(a) shows a model of the Ni/PCS-4 catalyst. The outside surface of the catalyst was black because of the loading of Ni particles. Its inside was still white because there were no Ni particles. The thickness of black catalyst layer was approximately 500 μm. It was due to the high catalytic activity of Ni particles for the $NaBH_4$ so that the $NaBH_4$ could not enter the interior of the Ni/PCS-4. The XRD patterns of PCS and Ni/PCS outside surface were analyzed and the results were shown in Fig. 1(b). All the reflections of the samples provided the diffraction patterns for the Al_2O_3 (PDF-ICDD 77–2135), rutile TiO_2 (PDF-ICDD 77–446), SiO_2 (PDF-ICDD 86–1562) and $NaAlSiO_4$ (PDF-ICDD 11–220). The complex diffraction patterns were due to the complexity of raw material components. As well known, the raw materials of glass powder contained PbO, MgO and etc, but no diffraction peaks attributed to Pb or Mg species were detected in the XRD patterns, implying that Pb or Mg species had a good dispersion in the Ni/PCS samples or existed as the burr peaks. The diffraction peaks attributed to Ni (PDF-ICDD 65–380) were detected in the Ni/PCS samples when the

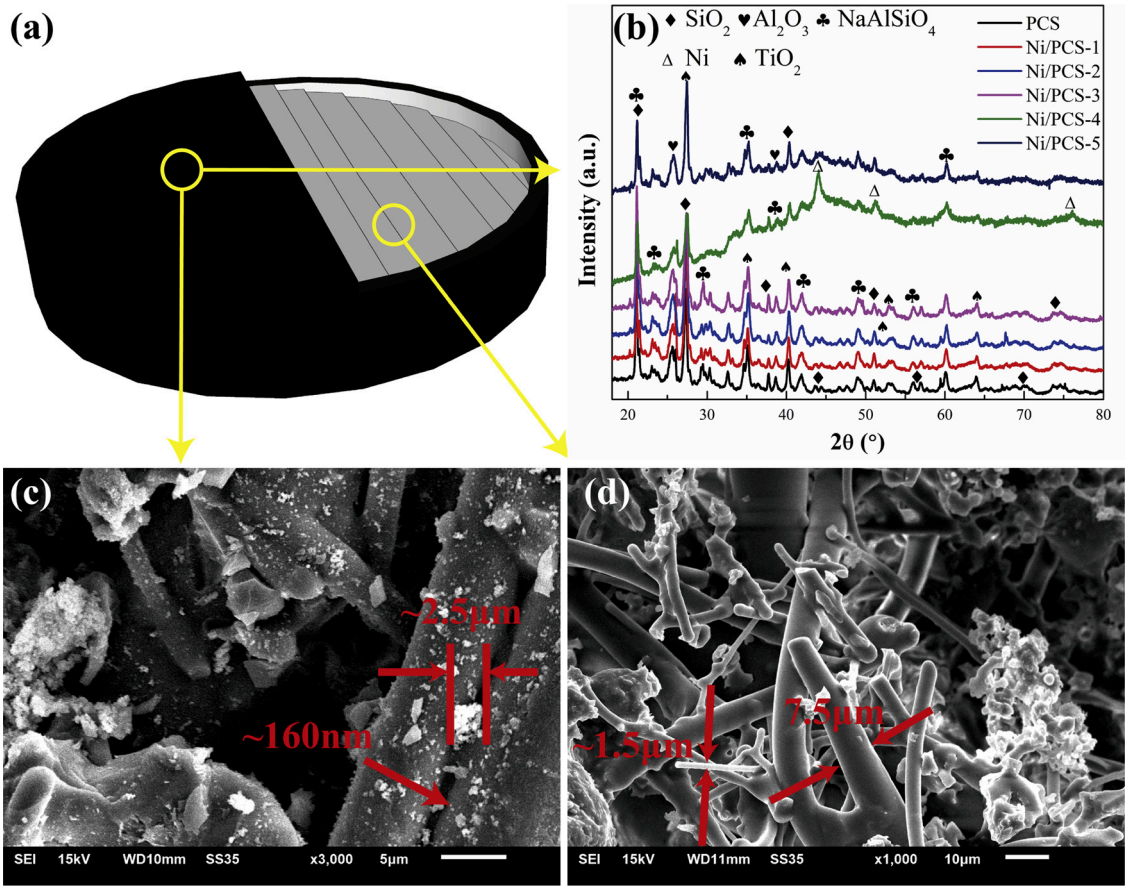

Fig. 1. (a) the model of Ni/PCS-4 catalyst; (b) X-ray diffraction patterns of Ni/PCS reactors; (c) SEM micrograph of Ni/PCS-4 outside surface and (d) SEM micrograph of Ni/PCS-4 inside surface.

Ni^0 was loaded in the catalyst. In addition, the intensity ratio of Ni/SiO_2 exhibited a parabolic trend, this was primarily due to a relative increase in the amount of Ni with the increase of $NiCl_3$ concentrations. Furthermore, Ni/PCS-4 exhibited the lowest peaks for SiO_2 and the highest peaks for Ni. It indicated that the loading content of Ni increased with the increase of $NiCl_3$ concentration and not all particles were loaded on the PCS for Ni/PCS-5 reactor.

The SEM micrographs of Ni/PCS-4 outside and inside surface were shown in Fig. 1(c) and 1(d). It was noted that the interior consisted mainly of smooth fibers and massive solids. Fiber diameter was mainly about 1.5–7.5 μm. There was no big change for the fiber diameter when the Ni was loaded in the catalyst, indicating the physical structure had no change. However, fine burrs and particles appeared on the surface of the fiber with the loading of Ni. The Ni particle size was mainly between 160 nm and 2.5 μm, and the large particles were agglomerated by small particles. Furthermore, the energy spectrums of Ni/PCS-4 were conducted to obtain the element content on the outside surface and interior (Fig. S1 and Fig. S2). It could be seen that there were O, Na, Mg, Al, Si, Ca, Ti and Pb elements and no Ni in the interior of Ni/PCS-4. Corresponding to this, the Ni and Cl elements were loading on the outside surface. It verified that the Ni was present on the outside surface of the Ni/PCS-4 catalyst and all the elements were evenly distributed in the catalyst.

To further research the physical properties of Ni/PCS catalysts, the original layer and Ni layer of Ni/PCS were cut and characterized by the Raman and mercury intrusion method. Consistent with the XRD result, the Raman spectra was complex and there were many small peaks, which was due to the complex composition of the catalyst. As shown in Fig. 2(a), the six peaks were assigned to the SiO_2, which could be observed at 218, 281, 404, 477, 712 and 772 cm^{-1} [44]. The bands located at 388, 503, 552, and 661 cm^{-1} was assigned to the Al_2O_3 [45,46]. The band located at 1002 cm^{-1} was assigned to the NiO [47]. The presence of NiO was likely due to NiO/hydroxide formation during catalyst processing when exposed to air. In addition, the Raman spectra demonstrated that Ni/PCS catalysts showed a positive shift in comparison with PCS. The shift corresponded to an increase in the number of surface oxygen vacancies [48]. Moreover, the Raman spectral intensity of Al_2O_3 and SiO_2 decreased significantly with the loading of Ni, indicating that Ni and NiO covered the Al_2O_3 and SiO_2. As shown in Fig. 2(b), the pore distribution of PCS was 2 − 50 μm and the most of the pore was 15 − 50 μm. The median pore of PCS was 28.9 μm and the bulk density (calculated by the mercury intrusion method) was 0.955 $g{\cdot}cm^{-3}$. By contrast, the loading of NiNPs decreased the pore distribution in the range of 2 − 50 μm, especially 20 − 30 μm. It indicated that the NiNPs were mainly supported on the pore (20 − 30 μm) surface. In addition, the pore at 10 − 30 nm generated with the loading of NiNPs, which was due to the interspace of the NiNPs. The bulk density of the Ni layer for Ni/PCS-4 increased to 1.214 $g{\cdot}cm^{-3}$ because Ni was a relatively heavy metal. However, the Ni layer was so thin that the bulk density of integral Ni/PCS-4 would not increase by 0.259 $g{\cdot}cm^{-3}$. Furthermore, the pores of all the PCS and Ni/PCS catalyst were relatively large allowing excellent filtered water performance and guaranteeing excellent catalytic performance of the Ni/PCS reactors.

To determine the loading content of Ni particles and other physical properties, the weighing method and Archimedes principle were employed. The detail information was shown in Table S1 and Fig. 3. As shown in Fig. 3(a), the loading content could be calculated by the weight difference before and after catalyst preparation process. Ni/PCS-4 had the maximum loading content (4.76%) and the loading content of Ni/PCS-5 was 3.45%. The concentration of $NiCl_3$ increased gradually from Ni/PCS-1 to Ni/PCS-5 when preparing the catalyst, but the loading of Ni/PCS-5 was smaller than that of Ni/PCS-4. This should be because the generated Ni particles increased gradually in size when the concentration of $NiCl_3$ was too high, so that the Ni particles were easily detached from the catalyst surface. In other words, the concentration of $NiCl_3$ in the catalyst preparation had the maximum limit. The multiple loading processes must be carried out if the loading content of Ni needed to increase continuously. It was noted that there was a positive correlation between loading content of Ni and catalytic efficiency. Bulk density was also one of important physical properties for ceramic materials. As shown in Fig. 3(b), PCS had the minimum bulk density (0.972 $g{\cdot}cm^{-3}$) and the loading of Ni would increase the bulk density of Ni/PCS catalyst obviously. In addition, the bulk density increased when the loading content of Ni and Ni/PCS-4 exhibited the maximum value (0.991 $g{\cdot}cm^{-3}$). This was a result of Ni being a relatively heavy metal and the Ni particles displaying no porous structures like PCS. The tiny Ni particles were loaded on the outside surface and inner surface of the catalyst tunnel.

The apparent porosity and water absorption were also important properties for the catalytic efficiency in the field of water treatment. The contaminated water passed through the internal pores of the Ni/PCS reactor, reacted with Ni particles, and was filtered spontaneously by gravity. Therefore, larger apparent porosity and readily exposed active sites would be highly beneficial for the filtration of contaminated water. The better water absorption performance would ensure that more contaminated water was inside the Ni/PCS reactors and reacting at the same time. As shown in Fig. 3(c), PCS exhibited the maximum apparent porosity (63.78%) and the loading of Ni would decrease apparent porosity. It was because the loaded Ni particles can block part of the PCS pore or reduced the diameter of the PCS pore. However, Ni/PCS-4 still showed a high apparent porosity (62.82%). The high apparent porosity of Ni/PCS-4 guaranteed that the reactor had enough

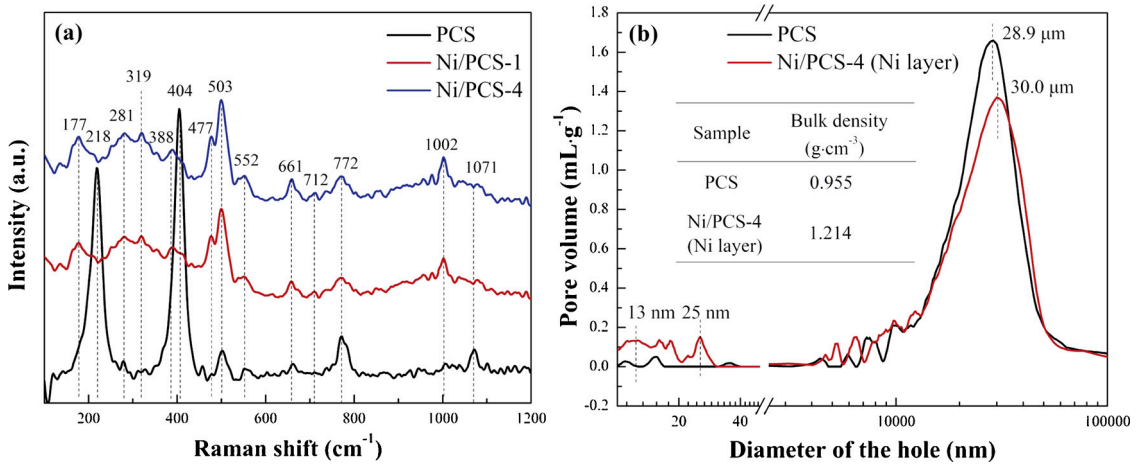

Fig. 2. (a) Raman spectra; (b) pore distribution of PCS catalysts.

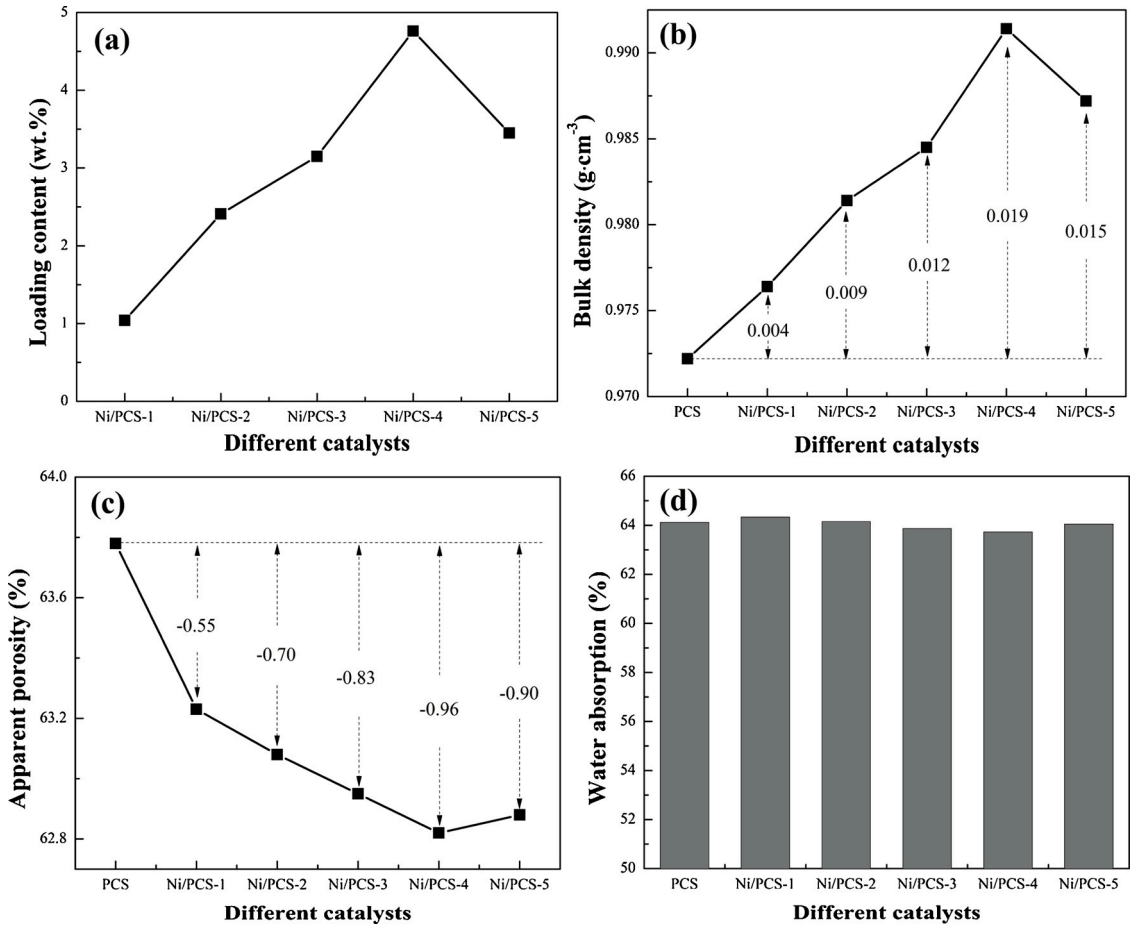

Fig. 3. (a) Loading content of Ni particles; (b) bulk density; (c) apparent porosity and (d) water absorption of Ni/PCS catalyst.

exposed active sites and the reacted liquid was more easily filtered. Fig. 3(d) described the water absorption of Ni/PCS reactors. The water absorption of PCS and Ni/PCS reactors was about 64%, demonstrating the loading of Ni had little effects on the water absorption. The high apparent porosity, water absorption, and the loading of Ni ensured that a large flow of contaminated water could pass through the reactor and reacted with the catalyst at the same time. It was concluded that this Ni/PCS reactor could dispose more contaminated water under the premise of excellent catalytic performance.

3.2. Surface element information

The surface composition and oxidation states of catalysts play an important role in the catalytic reduction, so the XPS was tested to investigate the surface properties of the catalysts. Fig. 4 and Fig. S3 showed the survey, Ni 2*p*, O 1*s*, Al 2*p* and Si 2*p* XPS high-resolution scans spectra of PCS, Ni/PCS-1, Ni/PCS-4 and Ni/PCS-5 catalysts. Table 1 showed the atomic distribution and percentage ratios of PCS and Ni/PCS catalysts. As shown in the Fig. 4(a), it could be seen that the PCS mainly consisted of Na, Ti, Al, Si, Pb, Ca, and O elements, which was due to the raw material of glass powder, wood powder and alumina fiber. This result was also consistent with that of XRD and elemental mapping. Compared with PCS, Ni/PCS catalyst had new elements (Ni, B and Cl), which was due to the loading of Ni and the vestigital of Cl^- and BO_2^-. Fig. 4(b) and Fig. S3(b) showed the representative Ni 2*p* spectra for the PCS, Ni/PCS-1, Ni/PCS-4 and Ni/PCS-5 catalysts. The result could be classified into two subsets including six different peaks: (1) the peaks located at 852.2 eV and 869.4 eV were metallic Ni (Ni^0) [49]; (2) the peaks located at 855.9 eV and 873.6 eV were Ni^{2+} species oxidation state; (3) the peaks located at 861.6 eV and 879.5 eV were satellite [50]. The presence of Ni^{2+} was likely to be NiO/hydroxide during catalyst processing when exposed to air [51]. The catalytic performance would be reduced slightly when NiO was generated. However, as shown in the XPS and catalytic reduction results, the catalytic efficiency of Ni^0 was still high after oxidation, indicating that the catalytic performance of NiO was not as good as that of Ni^0, but it was still active. In addition, the loading content of Ni (2.7 at%, 8.3 at% and 6.4 at%) by XPS test was much higher than that (1.04 wt%, 4.76 wt% and 3.45 wt%) by the weighing method. This was due to the adsorbed Ni^{2+} segregating to the surface of the PCS and reacting with $NaBH_4$ to form Ni^0. This resulted in a high concentration of Ni^0 on the catalyst surface and no Ni^0 inside the catalyst. Furthermore, the presence of NiO dense film prevented Ni^0 from continuing to oxidize, resulting in a higher Ni^0/Ni^{2+} molar ratio of Ni/PCS-4 than that of Ni/PCS-1 and Ni/PCS-5.

Fig. 4(c) and Fig. S3(c) showed the O 1*s* spectra for the PCS and Ni/PCS catalysts. The O 1*s* peaks could be fitted into two peaks referred to the chemisorbed oxygen (hereafter denoted as O_α) and the lattice oxygen (hereafter denoted as O_β) [52]. It was noted that the loading of Ni increased the percentage of O element and relative content of O_α. It was well known that surface chemisorbed oxygen was the most active oxygen and played an important role in catalytic reaction [53], which was one of the reasons why the catalytic activities decreased as Ni/PCS-4 > Ni/PCS-5 > Ni/PCS-1 > PCS. Fig. 4(d) and Fig. S3(d) showed the Al 2*p* spectra for the PCS and Ni/PCS catalysts. The Al 2*p* peak could be fitted into two peaks referred to Al $2p_{3/2}$ (located at 74.0 eV) and Al $2p_{1/2}$ (located at 74.9 eV). With the quantification of the peak areas of the spectra presented in Fig. 4(d), it was possible to estimate the thickness of the Al_2O_3 overlayer employing a multilayer approach that evaluated the signal attenuation due to scattering [54,55]. Therefore, the Al 2*p* photoemission intensity decreased with the increase of Ni

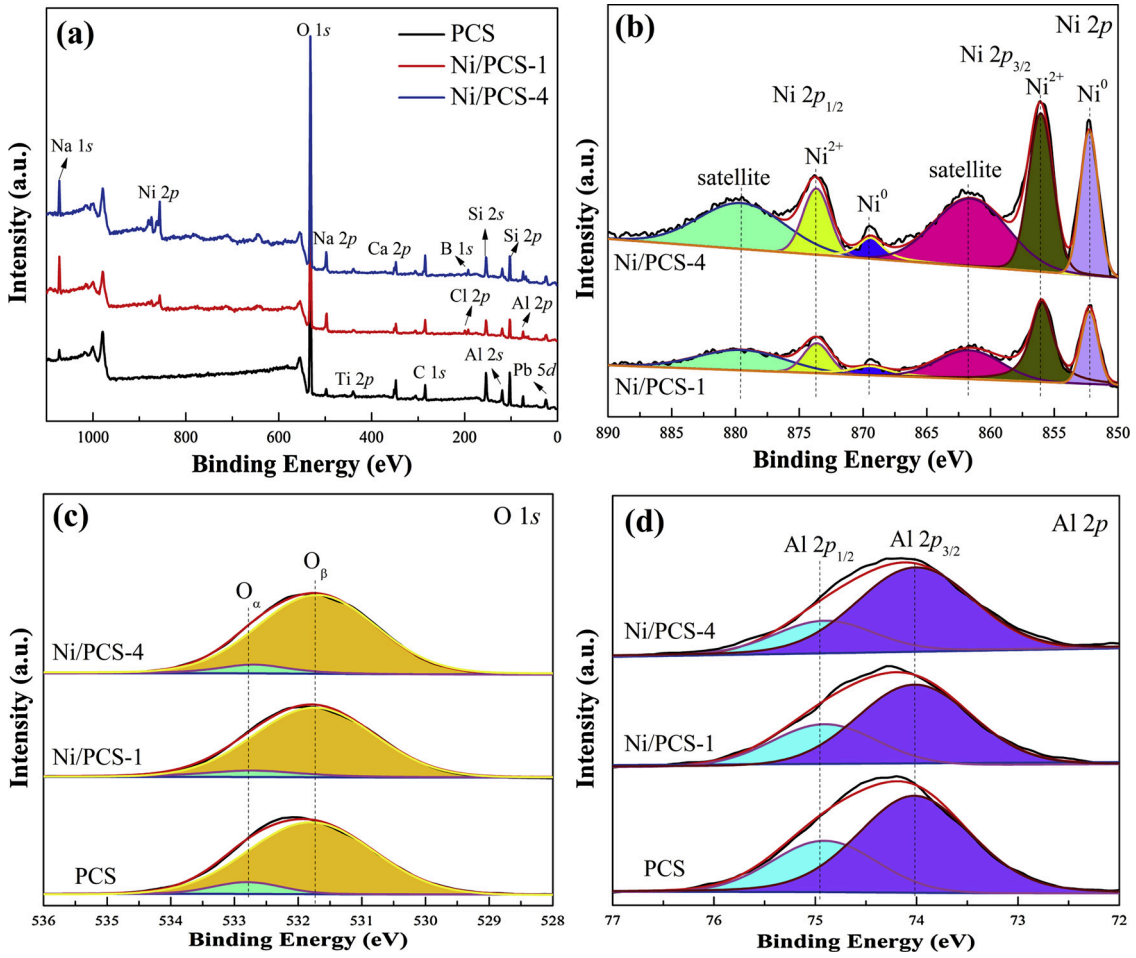

Fig. 4. (a) Survey; (b) Ni 2*p*; (c) O 1*s* and (d) Al 2*p* high-resolution scan spectra of PCS, Ni/PCS-1 and Ni/PCS-4 catalysts.

amount. As shown in Fig. S3(e), the Si 2*p* photoemission intensity also decreased with the increase of Ni amount, which was due to the overlay of Ni particles. Furthermore, the shift of peak to low binding energy indicated the strong interaction between Ni and Si. This resulted in a decrease in catalytic activities as Ni/PCS-4 > Ni/PCS-5 > Ni/PCS-1 > PCS.

3.3. Catalytic reduction

The continuous-flow catalysis was conducted by the Ni/PCS reactors and the diagrammatic drawing was shown in Fig. 5. From the Fig. 5(a), the Ni/PCS catalyst (cylinder, diameter of 22 mm, thickness of 10 mm) was tightly packed into a quartz tube. The injection syringe was equipped with a silicon tube and stacked at the micro-injection pump. The initial reaction solution (40 mL) was fed into the Ni/PCS reactor and the height of the reaction solution was kept by the micro-injection pump. The reacted solution was filtered by the Ni/PCS reactor and then trickled down by gravity. In this experiment, the injection speed was 2.67 mL·min^{-1} so the initial reaction solution (40 mL) was disposed equivalently in 15 min. Fig. 5(b) showed the UV–vis absorption spectra of a 5 mM 4-NP solution with 0.1 M $NaBH_4$ before and after feeding into the Ni/PCS-4 reactor. During this experiment, the yellow color of 4-NP/$NaBH_4$ solution faded and ultimately bleached with the treatment of Ni/PCS reactor. The characteristic peak intensity at 400 nm decreased and that at 300 nm increased after the reactor. Fig. S4 showed the peak position shifted from 315 nm to 400 nm when the $NaBH_4$ was added into 4-NP solution. It was determined from literature that the peak at 400 nm represented the 4-NP and the peak at about 300 nm represented 4-AP [56]. It was also noted that the value of TOC had no great change before and after the reaction (Fig. S5). Meaning, the 4-NP had been completely transformed to 4-AP with no other by-product ($HO\text{-}C_6H_4\text{-}NO_2 + BH_4^- \rightarrow HO\text{-}C_6H_4\text{-}NH_2 + BO_2^- + 2H_2$). Therefore, the change of peak intensity was caused by the transformation from 4-NP to 4-AP, and the Ni/PCS-4 reactor achieved 100 % conversion at the injection speed of 2.67 mL·min^{-1}.

The conversions versus 4-NP concentration for different Ni/PCS

Table 1
Atomic distribution and percentage of PCS and Ni/PCS catalysts.

Sample	Chemical composition (At%)				Relative content	
	Ni	O	Al	Si	$Ni^0/(Ni^{2+} + Ni^0)$	$O_\alpha/(O_\beta + O_\alpha)$
PCS	0	65.4	10.7	23.9	–	0.086
Ni/PCS-1	2.7	68.6	9.8	18.9	0.343	0.090
Ni/PCS-4	8.3	68.3	5.4	18.0	0.364	0.096
Ni/PCS-5	6.4	68.3	7.0	18.3	0.361	0.093

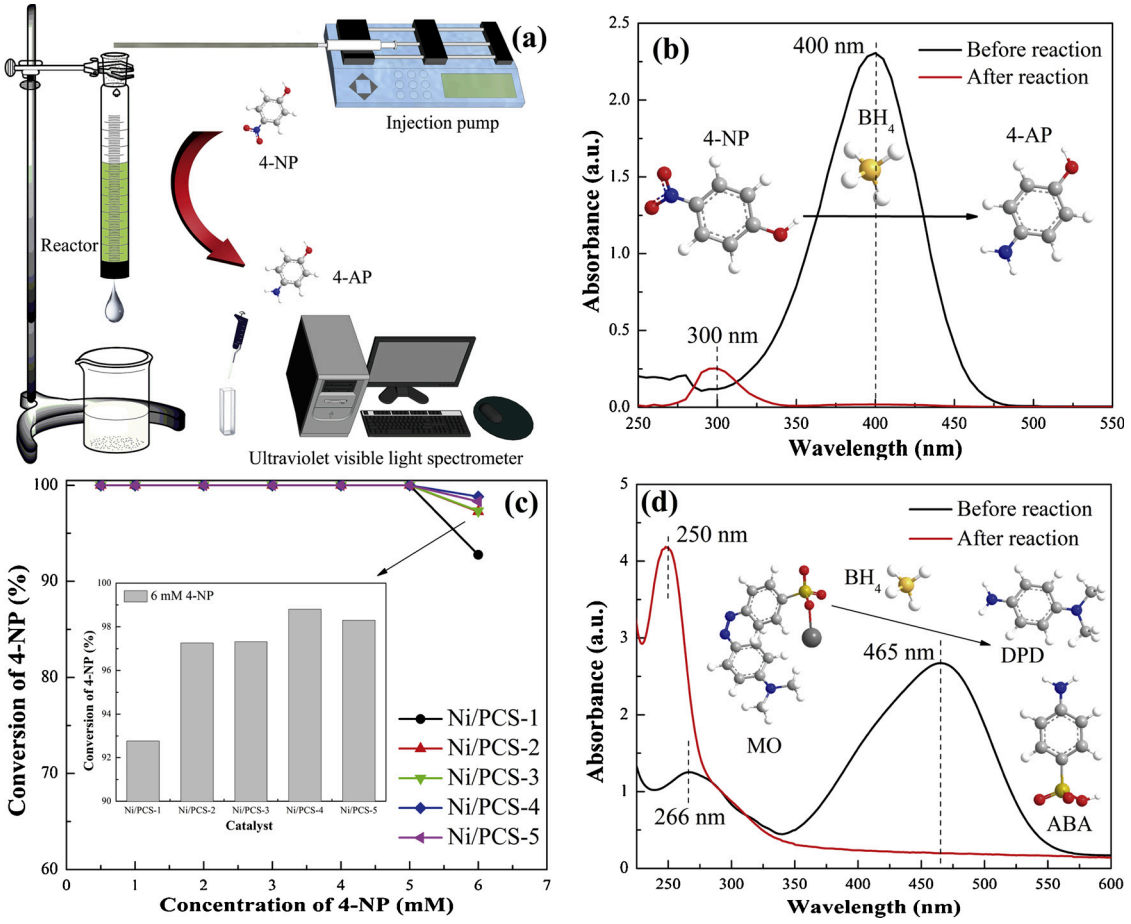

Fig. 5. Continuous-flow catalysis by the Ni/PCS reactors. (a) the catalytic system containing the Ni/PCS reactor; (b) UV–vis absorption spectra of 5 mM 4-NP solution with 0.1 M $NaBH_4$ before and after feeding into the Ni/PCS-4 reactor; (c) 4-NP conversions versus 4-NP concentration for different Ni/PCS reactors; (d) UV–vis absorption spectra of 0.3 mM MO solution with 30 mM $NaBH_4$ before and after feeding into the Ni/PCS-4 reactor.

reactors were shown in Fig. 5(c). All the catalytic efficiencies of Ni/PCS reactors could reach 100% at the injection speed of 2.67 mL·min^{-1} when the 4-NP concentration was lower than 5 mM, indicating the Ni/PCS reactor exhibited higher catalytic activity than the reactor based on AuNPs-anchored paper [15]. The efficiency of AuNPs-anchored paper reactor reached 100% when the speed was only lower than 0.05 mL·min^{-1}. In addition, the catalytic efficiency decreased with the increase of 4-NP concentration. It was because the effective collision frequency on the Ni particles surface decreased when the injection speed remained 2.67 mL·min^{-1} and the 4-NP concentration increased. When the 4-NP concentration was 6 mM, there was a significant difference among these Ni/PCS reactors. The Ni/PCS-4 exhibited the best catalytic performance (98.8%) at 2.67 mL·min^{-1}. The maximum conversion of Ni/PCS reactors decreased as Ni/PCS-4 > Ni/PCS-5 > Ni/PCS-3 > Ni/PCS-2 > Ni/PCS-1. The conversion of the Ni/PCS reactor is basically positively correlated with the loading content of Ni particles. The main reason for higher conversion of Ni/PCS-4 than that of Ni/PCS-5 may also be due to the loading content and the size of Ni particles. Many black Ni particles suspended in solution when the PCS (absorbed Ni^{2+}) was added into 50 mL sodium borohydride to prepare the Ni/PCS-5 catalyst. In other words, the concentration of $NiCl_3$ solution could not be too high or the Ni particles would be agglomerated and not all particles were loaded on the PCS. In order to confirm the superiority of Ni/PCS reactor in the environmental catalysis, Ni/PCS-4 was applied for MO reduction. From the Fig. 5(d), the peak at 465 nm was attributed to the n-π* transition of azo structure in MO molecule. The peak at 266 nm was attributed to the π-π* transition of the benzene ring conjugated system in MO molecule. These two peaks disappeared and the yellow solution transformed to a colorless one while a new peak at 250 nm appeared. It suggested that MO reduced in the presence of Ni particles and degraded into new small molecule products [57]. Therefore, the catalytic efficiencies of Ni/PCS-4 reactor reached 100% at the injection speed of 2.67 mL·min^{-1} when the MO concentration was 0.3 mM. These results further substantiate Ni/PCS-4 as an excellent reactor for the water treatment.

The great advantages of heterogeneous catalyst were the easy separation from the reaction medium and the reusability in consecutive runs [58]. In the present case, the reusability of Ni/PCS-4 was investigated (Fig. 6) and the used sample was washed and dried for subsequent experiment. The concentrations of 4-NP and MO for recycling were 5 mM and 0.3 mM, respectively. As shown in Fig. 6, the catalytic efficiencies of 4-NP and MO reduction had no great change after 10 recycling times. The Ni^0 would be oxidized gradually when the catalyst was exposed to air so that the catalytic efficiency decreased slightly. Furthermore, the conversion rates of Ni/PCS-4 could reach 99.6% (4-NP) and 99.4% (MO) at the tenth recycling time. Compared with other catalysts, such as Cu_2O@h-BN (50% activity loss after 4 recycling times) [59], NiNPs in hydrogel network (25% activity loss after 5 recycling times) [60], and Ag/CH-FP (10% activity loss after 4 recycling times) [61], the Ni/PCS-4 exhibited a significantly better reusability. To summarize, the Ni/PCS-4 had excellent reusability, which could be applied to the practical application. Fig. S6 showed the potential reaction mechanism of 4-NP transformation to 4-AP and the transformation was a six electron process in the presence of $NaBH_4$ [25]. The NiNPs on the PCS transferred $NaBH_4$ to active hydrogen species and adsorbed on the catalyst surface. Afterwards, the nitro

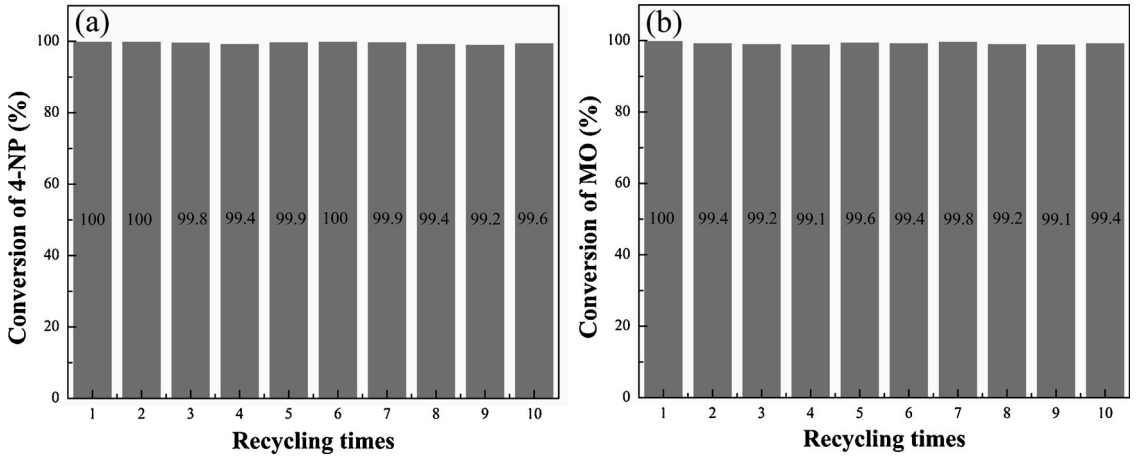

Fig. 6. Effect of recycling time on 4-NP and MO reduction over Ni/PCS-4 reactor.

groups of 4-NP molecules presented in the interfacial region would be transferred to amino groups with the induction of adsorbed hydrogen species [62].

4. Conclusions

In this work, a facile approach to synthesize Ni particles over the porous ceramic sheet was developed. The Ni/PCS catalyst was fabricated as a continuous-flow reactor. The Ni/PCS reactor was used for the first time in the process of nitroaromatic compounds and methyl orange reduction. Different samples were characterized structurally and morphologically by XRD, SEM, XPS, Raman, element mapping, mercury intrusion method, and Archimedes principle. For Ni/PCS, it was found that Ni existed in the form of nanoparticle structures with the particle size mainly between 160 nm and 2.5 μm. The PCS could maintain the structure in non-ideal conditions and the strong interaction guaranteed that the Ni particles durable adherence to PCS surface. Therefore, for the optimum reactor (Ni/PCS-4), both the conversion of 4-NP (5 mM) and MO (0.3 mM) reached nearly 100% at the injection speed of 2.67 $mL{\cdot}min^{-1}$. It also kept the conversion of 100% after 10 recycling times. Moreover, the loading of Ni increased the concentrations of chemisorbed oxygen. The high apparent porosity of Ni/PCS guaranteed that the reactor had enough exposed active sites and the reacted liquid was more easily filtered. Therefore, the Ni/PCS reactor had high catalytic efficiency and excellent reusability. While we have proven, the PCS supported Ni particles possess high catalytic efficiency and high reusability in the field of water treatment, the porous ceramic sheet could support other metal nanomaterial (such as Ag, Au, Pt and Pd) and pose potential for use in other fields of environmental catalysis. The universality and all of these advantages were favorable factors so that the PCS reactor could be used for wide practical applications.

Acknowledgements

We would like to acknowledge the financial support from the National Natural Science Foundation of China (51772149), National Key Research and Development Program of China (2016YFC0205500), Priority Academic Program Development of Jiangsu Higher Education Institutions (PAPD), the U.S. NSF-PREM program (DMR 1827745), and the National Institute of Allergy and Infectious Disease of the NIH (R21AI107415).

Appendix A. Supplementary data

Supplementary material related to this article can be found, in the online version, at doi:https://doi.org/10.1016/j.cattod.2019.12.006.

References

[1] H. Seo, A.F. Liu, T.F. Jamison, Direct beta-selective hydrocarboxylation of styrenes with CO_2 enabled by continuous flow photoredox catalysis, J. Am. Chem. Soc. 139 (2017) 13969–13972.
[2] M. Zhang, L.J. Wei, H. Chen, Z.P. Du, B.P. Binks, H.Q. Yang, Compartmentalized droplets for continuous flow liquid-liquid interface catalysis, J. Am. Chem. Soc. 138 (2016) 10173–10183.
[3] L. Tian, H.L. Jiang, P.H. Chen, Q. Wang, P.P. Niu, Y.M. Shi, M.H. Zhou, Y.C. Qing, X.B. Luo, A novel GO/PNIPAm hybrid with two functional domains can simultaneously effectively adsorb and recover valuable organic and inorganic resources, Chem. Eng. J. 343 (2018) 607–618.
[4] B.P. Mason, K.E. Price, J.L. Steinbacher, A.R. Bogdan, D.T. McQuade, Greener approaches to organic synthesis using microreactor technology, Chem. Rev. 107 (2007) 2300–2318.
[5] R.L. Huang, H.X. Zhu, R.X. Su, W. Qi, Z.M. He, Catalytic membrane reactor immobilized with alloy nanoparticle-loaded protein fibrils for continuous reduction of 4-nitrophenol, Environ. Sci. Technol. 50 (2016) 11263–11273.
[6] D. Webb, T.F. Jamison, Continuous flow multi-step organic synthesis, Chem. Sci. 1 (2010) 675–680.
[7] L.W. Miller, F.D. Pagani, S.D. Russell, R. John, A.J. Boyle, K.D. Aaronson, J.V. Conte, Y. Naka, D. Mancini, R.M. Delgado, T.E. MacGillivray, D.J. Farrar, O.H. Frazier, I.I.C.I. HeartMate, Use of a continuous-flow device in patients awaiting heart transplantation, New England J. Med. Surg. Collat. Branches Sci. 357 (2007) 885–896.
[8] M.S. Slaughter, J.G. Rogers, C.A. Milano, S.D. Russell, J.V. Conte, D. Feldman, B. Sun, A.J. Tatooles, R.M. Delgado, J.W. Long, T.C. Wozniak, W. Ghumman, D.J. Farrar, O.H. Frazier, I.I.I. HeartMate, Advanced heart failure treated with continuous-flow left ventricular assist device, New England J. Med. Surg. Collat. Branches Sci. 361 (2009) 2241–2251.
[9] N. Pamme, Continuous flow separations in microfluidic devices, Lab Chip 7 (2007) 1644–1659.
[10] H.F. Liang, F. Meng, M. Caban-Acevedo, L.S. Li, A. Forticaux, L.C. Xiu, Z.C. Wang, S. Jin, Hydrothermal continuous flow synthesis and exfoliation of NiCo layered double hydroxide nanosheets for enhanced oxygen evolution catalysis, Nano Lett. 15 (2015) 1421–1427.
[11] F. Ferlin, S. Santoro, L. Ackermann, L. Vaccaro, Heterogeneous C-H alkenylations in continuous-flow: oxidative palladium-catalysis in a biomass-derived reaction medium, Green Chem. 19 (2017) 2510–2514.
[12] P. Poechlauer, J. Manley, R. Broxterman, B. Gregertsen, M. Ridemark, Continuous processing in the manufacture of active pharmaceutical ingredients and finished dosage forms: an industry perspective, Org. Process Res. Dev. 16 (2012) 1586–1590.
[13] J. Wegner, S. Ceylan, A. Kirschning, Ten key issues in modern flow chemistry, Chem. Commun. (Camb.) 47 (2011) 4583–4592.
[14] J. Britton, C.L. Raston, Multi-step continuous-flow synthesis, Chem. Soc. Rev. 46 (2017) 1250–1271.
[15] H. Koga, N. Namba, T. Takahashi, M. Nogi, Y. Nishina, Renewable wood pulp paper reactor with hierarchical micro/nanopores for continuous-flow nanocatalysis, ChemSusChem 10 (2017) 2560–2565.
[16] M.A. Mahmoud, R. Narayanan, M.A. El-Sayed, Enhancing colloidal metallic nanocatalysis: sharp edges and corners for solid nanoparticles and cage effect for hollow ones, Acc. Chem. Res. 46 (2013) 1795–1805.
[17] Z.Y. Jiang, X.H. Zhang, Z.M. Yuan, J.C. Chen, B.B. Huang, D.D. Dionysiou, G.H. Yang, Enhanced photocatalytic CO_2 reduction via the synergistic effect between Ag and activated carbon in TiO_2/AC-Ag ternary composite, Chem. Eng. J. 348 (2018) 592–598.
[18] S. Rajendran, D. Manoj, K. Raju, D.D. Dionysiou, M. Naushad, F. Gracia, L. Cornejo, M.A. Gracia-Pinilla, T. Ahamad, Influence of mesoporous defect induced mixed-valent NiO (Ni^{2+}/Ni^{3+})-TiO_2 nanocomposite for non-enzymatic glucose biosensors,

Sensors Actuators B: Chem. 264 (2018) 27–37.
[19] X. Wei, W. Zhou, S.T. Sanjay, J. Zhang, Q. Jin, F. Xu, D.C. Dominguez, X. Li, Multiplexed instrument-free bar-chart SpinChip integrated with nanoparticle-mediated magnetic aptasensors for visual quantitative detection of multiple pathogens, Anal. Chem. 90 (2018) 9888–9896.
[20] G. Fu, S.T. Sanjay, W. Zhou, R.A. Brekken, R.A. Kirken, X. Li, Exploration of nanoparticle-mediated photothermal effect of TMB-H2O2 colorimetric system and its application in a visual quantitative photothermal immunoassay, Anal. Chem. 90 (2018) 5930–5937.
[21] G. Fu, S.T. Sanjay, M. Dou, X. Li, Nanoparticle-mediated photothermal effect enables a new method for quantitative biochemical analysis using a thermometer, Nanoscale 8 (2016) 5422–5427.
[22] S. Zhan, H. Zhang, Y. Zhang, Q. Shi, Y. Li, X. Li, Efficient NH_3-SCR removal of NO_x with highly ordered mesoporous $WO_3(\chi)$-CeO_2 at low temperatures, Appl. Catal. B: Environmental 203 (2017) 199–209.
[23] N. Agarwal, S.J. Freakley, R.U. McVicker, S.M. Althahban, N. Dimitratos, Q. He, D.J. Morgan, R.L. Jenkins, D.J. Willock, S.H. Taylor, C.J. Kiely, G.J. Hutchings, Aqueous Au-Pd colloids catalyze selective CH_4 oxidation to CH_3OH with O_2 under mild conditions, Science 358 (2017) 223–226.
[24] S.K. Katla, J. Zhang, E. Castro, R.A. Bernal, X.J. Li, Atomically precise $Au_{25}(SG)_{18}$ nanoclusters: rapid single-step synthesis and application in photothermal therapy, ACS Appl. Mater. Interfaces 10 (2018) 75–82.
[25] T. Kamal, S.B. Khan, A.M. Asiri, Nickel nanoparticles-chitosan composite coated cellulose filter paper: an efficient and easily recoverable dip-catalyst for pollutants degradation, Environ. Pollut. 218 (2016) 625–633.
[26] M. Khalil, E.S. Anggraeni, T.A. Ivandini, E. Budianto, Exposing TiO_2 (001) crystal facet in nano Au-TiO_2 heterostructures for enhanced photodegradation of methylene blue, Appl. Surf. Sci. 487 (2019) 1376–1384.
[27] Z.L. Yan, L.J. Fu, X.C. Zuo, H.M. Yang, Green assembly of stable and uniform silver nanoparticles on 2D silica nanosheets for catalytic reduction of 4-nitrophenol, Appl. Catal. B 226 (2018) 23–30.
[28] X. Li, X. Wang, S. Song, D. Liu, H. Zhang, Selectively deposited noble metal nanoparticles on Fe_3O_4/graphene composites: stable, recyclable, and magnetically separable catalysts, Chem.-Eur. J. 18 (2012) 7601–7607.
[29] R.L. Hartman, J.P. McMullen, K.F. Jensen, Deciding whether to go with the flow: evaluating the merits of flow reactors for synthesis, Angew. Chem.-Int. Edit. 50 (2011) 7502–7519.
[30] J. Li, F.C. Wu, L. Lin, Y. Guo, H.O. Liu, X.F. Zhang, Flow fabrication of a highly efficient Pd/UiO-66-NH_2 film capillary microreactor for 4-nitrophenol reduction, Chem. Eng. J. 333 (2018) 146–152.
[31] E.S. Gnanakumar, N. Chandran, I.V. Kozhevnikov, A. Grau-Atienza, E.V.R. Fernandez, A. Sepulveda-Escribano, N.R. Shiju, Highly efficient nickel-niobia composite catalysts for hydrogenation of CO_2 to methane, Chem. Eng. Sci. 194 (2019) 2–9.
[32] Q.J. Jin, Y.S. Shen, Y. Cai, L. Chu, Y.W. Zeng, Resource utilization of waste V_2O_5-based deNO_x catalysts for hydrogen production from formaldehyde and water via steam reforming, J. Hazard. Mater. 381 (2019) 120934.
[33] H. Mao, C.G. Ji, M.H. Liu, Z.Q. Cao, D.Y. Sun, Z.Q. Xing, X. Chen, Y. Zhang, X.M. Song, Enhanced catalytic activity of Ag nanoparticles supported on polyacrylamide/polypyrrole/graphene oxide nanosheets for the reduction of 4-nitrophenol, Appl. Surf. Sci. 434 (2018) 522–533.
[34] Y. Gu, Y.Q. Jiao, X.G. Zhou, A.P. Wu, B. Buhe, H.G. Fu, Strongly coupled Ag/TiO_2 heterojunctions for effective and stable photothermal catalytic reduction of 4-nitrophenol, Nano Res. 11 (2018) 126–141.
[35] Q.J. Jin, Y.S. Shen, L. Ma, Y.C. Pan, S.M. Zhu, J. Zhang, W. Zhou, X.F. Wei, X.J. Li, Novel TiO_2 catalyst carriers with high thermostability for selective catalytic reduction of NO by NH_3, Catal. Today 327 (2019) 279–287.
[36] F. Wei, C.F. Lu, F.Y. Wang, G.C. Yang, Z.X. Chen, J.Q. Nie, A novel functionalized porous polythiophene polymer network for Au catalyst deposition, Mater. Lett. 212 (2018) 251–255.
[37] X.Y. An, Y.D. Long, Y.H. Ni, Cellulose nanocrystal/hexadecyltrimethylammonium bromide/silver nanoparticle composite as a catalyst for reduction of 4-nitrophenol, Carbohydr. Polym. 156 (2017) 253–258.
[38] T. Zeng, K.L. Ziegelgruber, Y.P. Chin, W.A. Arnold, Pesticide processing potential in prairie pothole porewaters, Environ. Sci. Technol. 45 (2011) 6814–6822.
[39] C. Lin, G. Wu, H. Li, Y. Geng, G. Xie, J. Yang, B. Liu, J. Jin, Rh nanoparticles supported on ultrathin carbon nanosheets for high-performance oxygen reduction reaction and catalytic hydrogenation, Nanoscale 9 (2017) 1834–1839.
[40] V.K. Gupta, M.L. Yola, T. Eren, F. Kartal, M.O. Çağlayan, N. Atar, Catalytic activity of Fe@Ag nanoparticle involved calcium alginate beads for the reduction of nitrophenols, J. Mol. Liq. 190 (2014) 133–138.
[41] B. Wang, X.L. Lv, D. Feng, L.H. Xie, J. Zhang, M. Li, Y. Xie, J.R. Li, H.C. Zhou, Highly stable Zr(IV)-based metal-organic frameworks for the detection and removal of antibiotics and organic explosives in water, J. Am. Chem. Soc. 138 (2016) 6204–6216.
[42] P.-T. Huong, B.-K. Lee, J. Kim, C.-H. Lee, Nitrophenols removal from aqueous medium using Fe-nano mesoporous zeolite, Mater. Des. 101 (2016) 210–217.
[43] P. Garcia, M. Malacria, C. Aubert, V. Gandon, L. Fensterbank, Gold-catalyzed cross-couplings: new opportunities for C–C bond formation, ChemCatChem 2 (2010) 493–497.
[44] A. Khamkongkaeo, A. Bootchanont, W. Klysubun, P. Amonpattaratkit, T. Boonchuduang, N. Tuchinda, T. Phetrattanarangsi, N. Nuntawong, S. Kuimalee, B. Lohwongwatana, Effect of phosphate compound on physical and mechanical properties of SiO_2 ceramic, Ceram. Int. 45 (2019) 1356–1362.
[45] K.M. Paradowska, E. Przezdziecka, E. Placzek-Popko, E. Zielony, M. Stachowicz, A. Kozanecki, Effect of annealing on photoluminescence and Raman scattering of Sb-doped ZnO epitaxial layers grown on a-Al_2O_3, J. Alloys. Compd. 774 (2019) 1160–1167.
[46] R. Cuscó, E. Alarcón-Lladó, J. Ibanez, L. Artús, J. Jimenez, B. Wang, M.J. Callahan, Temperature dependence of Raman scattering in ZnO, Phys. Rev. B 75 (2007) 165202.
[47] V. Ganesh, L. Haritha, M. Anis, M. Shkir, I.S. Yahia, A. Singh, S. AlFaify, Structural, morphological, optical and third order nonlinear optical response of spin-coated NiO thin films: an effect of N doping, Solid State Sci. 86 (2018) 98–106.
[48] X.R. Li, J.G. Wang, Y. Men, Z.F. Bian, TiO_2 mesocrystal with exposed (001) facets and CdS quantum dots as an active visible photocatalyst for selective oxidation reactions, Appl. Catal. B 187 (2016) 115–121.
[49] Q.J. Jin, Y.S. Shen, X.J. Li, Y.W. Zeng, Resource utilization of waste deNO_x catalyst for continuous-flow catalysis by supported metal reactors, Mol. Catal. 480 (2020) 110634.
[50] Y.K. Zhang, Z.L. Jin, H. Yuan, G.R. Wang, B.Z. Ma, Well-regulated nickel nanoparticles functional modified ZIF-67 (Co) derived Co_3O_4/CdS p-n heterojunction for efficient photocatalytic hydrogen evolution, Appl. Surf. Sci. 462 (2018) 213–225.
[51] G. Han, Y.H. Jin, R.A. Burgess, N.E. Dickenson, X.M. Cao, Y. Sun, Visible-light-driven valorization of biomass intermediates integrated with H_2 production catalyzed by ultrathin Ni/CdS nanosheets, J. Am. Chem. Soc. 139 (2017) 15584–15587.
[52] W. Yan, Y.S. Shen, Q.J. Jin, Y.L. Liu, X.H. Li, Promotional effect of molybdenum additives on catalytic performance of CeO_2/Al_2O_3 for selective catalytic reduction of NO_x, Catal. Lett. 146 (2016) 1221–1230.
[53] L.F. Liotta, M. Ousmane, G. Di Carlo, G. Pantaleo, G. Deganello, G. Marcì, L. Retailleau, A. Giroir-Fendler, Total oxidation of propene at low temperature over Co3O4–CeO2 mixed oxides: role of surface oxygen vacancies and bulk oxygen mobility in the catalytic activity, Appl. Catal. A Gen. 347 (2008) 81–88.
[54] D. Cabrera-German, G. Molar-Velázquez, G. Gómez-Sosa, W. de la Cruz, A. Herrera-Gomez, Detailed peak fitting analysis of the Zn 2p photoemission spectrum for metallic films and its initial oxidation stages, Surf. Interface Anal. 49 (2017) 1078–1087.
[55] A. Herrera-Gomez, F.S. Aguirre-Tostado, P.G. Mani-Gonzalez, M. Vazquez-Lepe, A. Sanchez-Martinez, O. Ceballos-Sanchez, R.M. Wallace, G. Conti, Y. Uritsky, Instrument-related geometrical factors affecting the intensity in XPS and ARXPS experiments, J. Electron. Spectrosc. Relat. Phenom. 184 (2011) 487–500.
[56] J.J. Lv, S.S. Li, A.J. Wang, L.P. Mei, J.R. Chen, J.J. Feng, Monodisperse Au-Pd bimetallic alloyed nanoparticles supported on reduced graphene oxide with enhanced electrocatalytic activity towards oxygen reduction reaction, Electrochim. Acta 136 (2014) 521–528.
[57] X.T. Zhang, J.Q. Wan, K.Z. Chen, S.X. Wang, Controlled synthesis of spherical and cubic magnetite nanocrystal clusters, J. Cryst. Growth 372 (2013) 170–174.
[58] Y.Y. Yue, H.Y. Liu, P. Yuan, C.Z. Yu, X.J. Bao, One-pot synthesis of hierarchical FeZSM-5 zeolites from natural aluminosilicates for selective catalytic reduction of NO by NH_3, Sci. Rep. 5 (2015) 10.
[59] C. Huang, W. Ye, Q. Liu, X. Qiu, Dispersed Cu_2O octahedrons on h-BN nanosheets for p-nitrophenol reduction, ACS Appl. Mater. Interfaces 6 (2014) 14469–14476.
[60] N. Sahiner, H. Ozay, O. Ozay, N. Aktas, New catalytic route: hydrogels as templates and reactors for in situ Ni nanoparticle synthesis and usage in the reduction of 2- and 4-nitrophenols, Appl. Catal. A Gen. 385 (2010) 201–207.
[61] I. Ahmad, T. Kamal, S.B. Khan, A.M. Asiri, An efficient and easily retrievable dip catalyst based on silver nanoparticles/chitosan-coated cellulose filter paper, Cellulose 23 (2016) 3577–3588.
[62] J.J. Lv, A.J. Wang, X.H. Ma, R.Y. Xiang, J.R. Chen, J.J. Feng, One-pot synthesis of porous Pt–Au nanodendrites supported on reduced graphene oxide nanosheets toward catalytic reduction of 4-nitrophenol, J. Mater. Chem. A Mater. Energy Sustain. 3 (2015) 290–296.